Supplementary Materials

An integrated bifunctional metamaterial perfect absorber for high-efficient broadband absorption and narrowband refractive index detection

Yilin Zuo[1,2], Weijia Han[1,2,*], Guochao Wei[1,2], Kang Du[1,2], Yan Liu[1,2], Shengxiang Wang[1,2]

[1]State Key Laboratory of New Textile Materials and Advanced Processing Technologies, Wuhan Textile University, Wuhan 430200, Hubei, China.
[2]School of Microelectronics, Wuhan Textile University, Wuhan 430200, Hubei, China.

Correspondence to: Assoc. Prof. Weijia Han, Prof. Shengxiang Wang, School of Microelectronics, Wuhan Textile University, Wuhan 430200, Hubei, China. E-mail: wjhan@wtu.edu.cn; shxwang@wtu.edu.cn

1. Mesh Convergence Analysis

To ensure numerical reliability of the simulations, mesh convergence analyses were performed by varying the mesh size from 8 nm to 2 nm. The corresponding narrowband and broadband absorption spectra are presented in Figs. S1 and S2, and the extracted characteristic parameters are summarized in Tables S1 and S2.

For the narrowband absorber, the resonance wavelength and peak absorptivity gradually converged as the mesh was refined. As listed in Table S1, the resonance wavelength was 959.96, 955.32, 948.40, 948.10, and 947.18 nm for mesh sizes of 8, 6, 4, 3, and 2 nm, respectively, while the corresponding peak absorptivity was 99.03%, 99.14%, 99.20%, 99.23%, and 99.26%. In particular, when the mesh size was reduced from 3 nm to 2 nm, the resonance wavelength changed by only 0.92 nm and the peak absorptivity changed by only 0.03%, indicating that the narrowband response was already well converged at 3 nm.

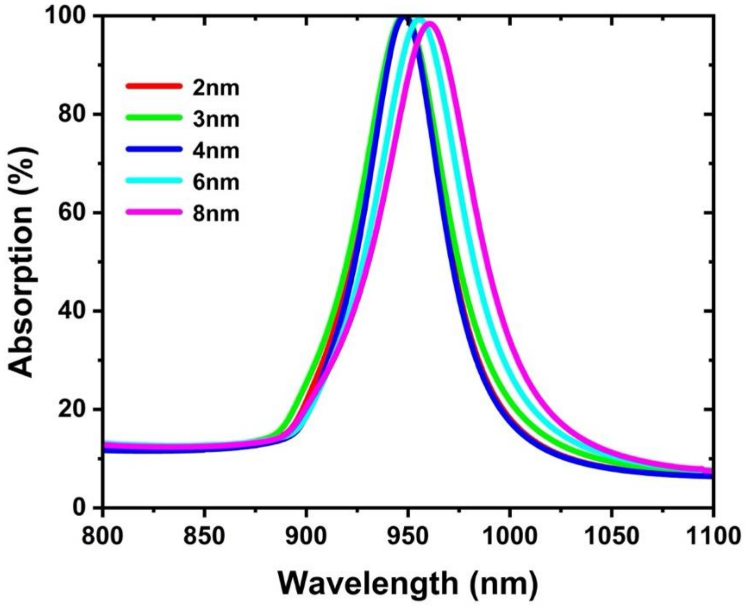

Figure S1. Calculated narrowband absorption spectra with setting different mesh size of 2, 3, 4, 6, and 8 nm.

Table S1. Resonance wavelength and the peak absorptivity of the calculated narrowband absorption spectra in Fig. S1 with setting different mesh size

Mesh size (nm)	2	3	4	6	8
Resonance wavelength (nm)	947.18	948.1	948.4	955.32	959.96
Peak absorptivity (%)	99.26	99.23	99.20	99.14	99.03

For the broadband absorber, a similar convergence trend was observed. As summarized in Table S2, the high-absorptivity bandwidth above 90% was 1456, 1493, 1507, 1500, and 1502 nm for mesh sizes of 8, 6, 4, 3, and 2 nm, respectively, and the corresponding average absorptivity was 95.60%, 97.04%, 97.26%, 97.48%, and 97.47%. The three characteristic absorption peaks also showed only small variations for the 2 and 3 nm meshes: the peak positions were 914.7/914.2 nm, 1242.75/1243.6 nm, and 1972.2/1971.3 nm, while the corresponding peak absorptivity were 99.98%/99.91%, 99.03%/99.02%, and 99.46%/99.44%, respectively. These results confirm that the broadband spectral response is also well converged at a mesh size of 3 nm.

Based on the mesh convergence analyses, a mesh size of 3 nm was adopted for simulations, since it provides a great compromise between numerical accuracy and computational cost. The results demonstrate that the simulated absorption characteristics reported in this work are robust with respect to mesh discretization.

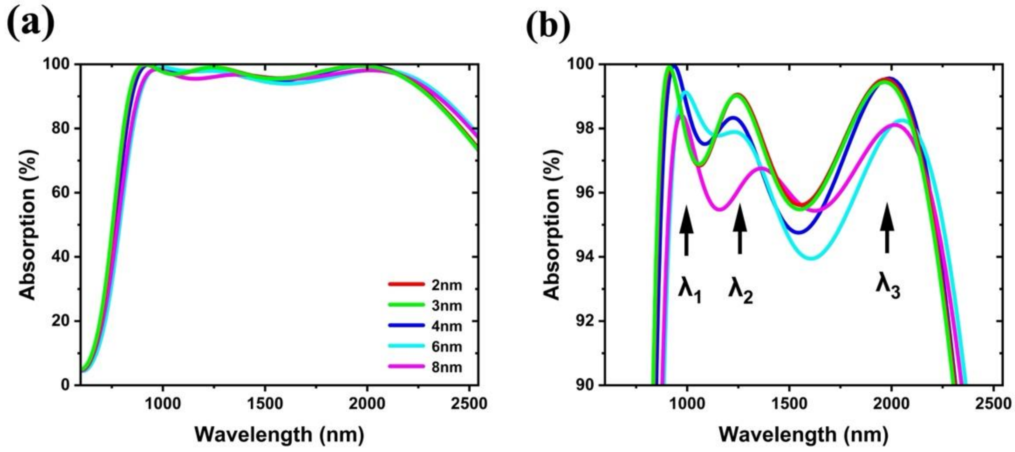

Figure S2. Calculated broadband absorption spectra with setting different mesh size of 2, 3, 4, 6, and 8 nm: (a) full spectral range and (b) enlarged view of the high-absorptivity region.

Table S2. Resonance wavelength and the peak absorptivity of the calculated broadband absorption spectra in Fig. S2 with setting different mesh size

Mesh size (nm)	**2**	**3**	**4**	**6**	**8**
High absorptivity bandwidth (>90%)	1502nm	1500nm	1507nm	1493nm	1456nm
Average absorptivity (%)	97.47	97.48	97.26	97.04	95.60
λ_1 wavelength (nm)	914.7	914.2	924.08	938.1	937.08
λ_1 absorptivity (%)	99.98	99.91	99.95	97.53	97.01
λ_2 wavelength (nm)	1242.75	1243.6	1229.5	1226.5	1260.1
λ_2 absorptivity (%)	99.03	99.02	98.33	97.89	96.59
λ_3 wavelength (nm)	1972.2	1971.3	1982.4	2027.4	2024.3
λ_3 absorptivity (%)	99.46	99.44	99.56	98.2	96.6

2.Lorentz-Drude Parameters of ZrN and FDTD Simulation Details

The optical permittivity of ZrN used in this work was described by the Lorentz-Drude model[1], and the complete fitted parameters are listed in Table S3. All electromagnetic simulations were carried out using the finite-difference time-domain (FDTD) method. To accurately resolve the geometrical features smaller than 20 nm, a mesh size of 3 nm was employed in the simulations. The adequacy of this discretization was further verified by the mesh-convergence analysis in Figs. S1 and S2 and Tables S2 and S3. Perfectly matched layer (PML) boundary conditions with 64 layers were applied along the z direction to minimize reflections from the simulation. The simulations were terminated when the residual electromagnetic energy in the computational domain decayed to the auto shutoff level of 1×10^{-8}, which ensured sufficient temporal convergence of the calculated spectra. The scattering parameters were extracted using the built-in S-parameter analysis group under the same excitation and monitor configuration used for all reported calculations.

Table S3. Lorentz–Drude model parameters for ZrN

Symbol	Parameter	Value	Unit
ω_p	Plasma Frequency	8.018	eV
ω_l	Resonance Frequency	5.48	eV
γ_p	Daming Constant of the Drude part	0.5192	eV
γ_l	Damping Constant	1.7369	eV
f_1	Oscillator Strength	2.4509	-
ϵ_b	Background permittivity	3.4656	-

3. Multipole decomposition analysis

To further clarify the resonance mechanism discussed in the main text, we performed a multipole decomposition analysis for the proposed BMA. Fig. S3 presents the normalized scattering power of the electric dipole (ED), magnetic dipole (MD), electric quadrupole (EQ), magnetic quadrupole (MQ), electric hexadecapole (EH), magnetic hexadecapole (MH), and the total contribution for the broadband and narrowband absorption modes. The results show that the broadband response is mainly dominated by the ED contribution with additional MD and weak EQ participation, whereas the narrowband resonance is primarily associated with coupled ED and MD contributions.

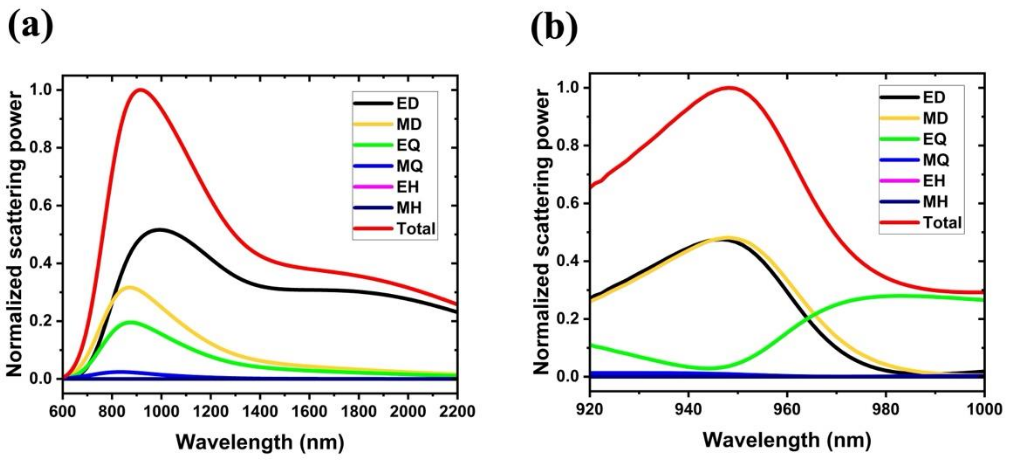

Figure S3. Multipole decomposition analysis of the proposed BMA: (a) broadband mode and (b) narrowband mode.

4. Layer-resolved absorption analysis of the proposed absorber

To clarify the physical origin of the absorption response, we performed a layer-resolved absorption analysis using the built-in Absorption Power analysis module. This analysis group evaluates the local electromagnetic power dissipation and integrates the absorbed power within selected material domains. By defining the Au, SiO_2, and ZrN regions separately, the absorption contribution of each layer was quantitatively extracted at the representative resonance wavelengths and over the broadband operating range. The corresponding results are summarized in Fig. S4 and Table S4.

For broadband absorption, the absorbed power is consistently dominated by the ZrN layer. At λ_1 = 914.2 nm, λ_2 = 1243.6 nm, and λ_3 = 1971.3 nm, the fraction of total absorbed power located in ZrN reaches 88.20%, 89.60%, and 90.63%, respectively. In contrast, the Au layer contributes only 0.38%, 0.25%, and 0.42% at these three resonances, indicating that the direct dissipation in Au plays only a minor role in the broadband absorption process. The SiO_2 layer contributes 11.41%, 10.15%, and 8.95%, respectively, suggesting that the dielectric layer participates in the modal energy distribution but is not the dominant loss medium. To further evaluate the overall broadband absorption behavior, the absorbed power was also integrated over the entire 600-2500 nm spectral range. The results show that 88.34% of the total absorbed power is dissipated in the ZrN layer, whereas only 1.02% is dissipated in Au and 10.64% in SiO_2. This broadband decomposition further confirms that ZrN is the main absorption layer across the full operating band.

For the narrowband mode, a similar trend is observed, but with even stronger localization of absorbed power in ZrN. At λ_4 = 948.1 nm, the ZrN layer accounts for 97.82% of the total absorbed power, whereas the Au layer contributes only 2.18%. This indicates that the near-perfect narrowband absorption originates almost entirely from loss within the ZrN layer once the resonant field is established in the multilayer cavity. Overall, the layer-resolved absorbed-power analysis directly demonstrates that the ZrN layer serves as the principal energy-dissipation medium in both the broadband and narrowband regimes. The Au layer mainly assists in shaping the resonant electromagnetic environment, but contributes little to the final absorption loss. Therefore, these results provide physical support for the interpretation that the observed response arises from resonant coupling and field confinement within the multilayer structure.

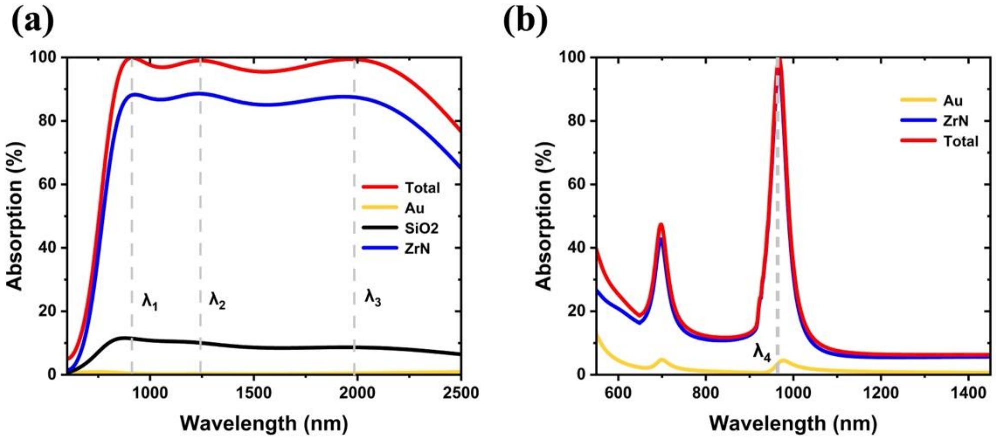

Figure S4. Layer-resolved absorbed-power distribution in the Au, SiO_2, and ZrN layers for the broadband resonances (a) and the narrowband resonance (b).

Table S4. Layer-resolved absorption analysis

Mode	Resonance	Wavelength	Au	SiO_2	ZrN
Broadband	λ_1	914.2	0.38 %	11.41 %	88.20 %
Broadband	λ_2	1243.6	0.25 %	10.15 %	89.60 %
Broadband	λ_3	1971.3	0.42 %	8.95 %	90.63 %

Broadband	Total	800-2300	1.02 %	10.64 %	88.34 %
Narrowband	λ_4	948.1	2.18 %	0 %	97.82 %

5. Fabrication feasibility and tolerance analysis

Given the structural complexity of the proposed BMA, its fabrication feasibility should be considered explicitly. The device requires double-sided nanopatterning, sub-20 nm critical features, and accurate front-to-back alignment, all of which impose nontrivial demands on nanofabrication. A fabrication route is briefly outlined as follows. First, alignment marks can be defined on the substrate to enable front-to-back registration during the subsequent double-sided patterning process. The metallic and dielectric nanostructures on the front and back surfaces can then be fabricated by sequential electron-beam lithography (EBL), thin-film deposition, and lift-off or etching steps. The ZrN functional layer may be deposited using a controllable thin-film technique such as reactive sputtering. In this way, the key geometric parameters can be defined by high-resolution lithography, while the layer thickness can be controlled during film growth. Although the combined requirements of sub-20 nm patterning and double-sided alignment remain challenging, such processes are in principle compatible with advanced nanofabrication capabilities reported in the literature.

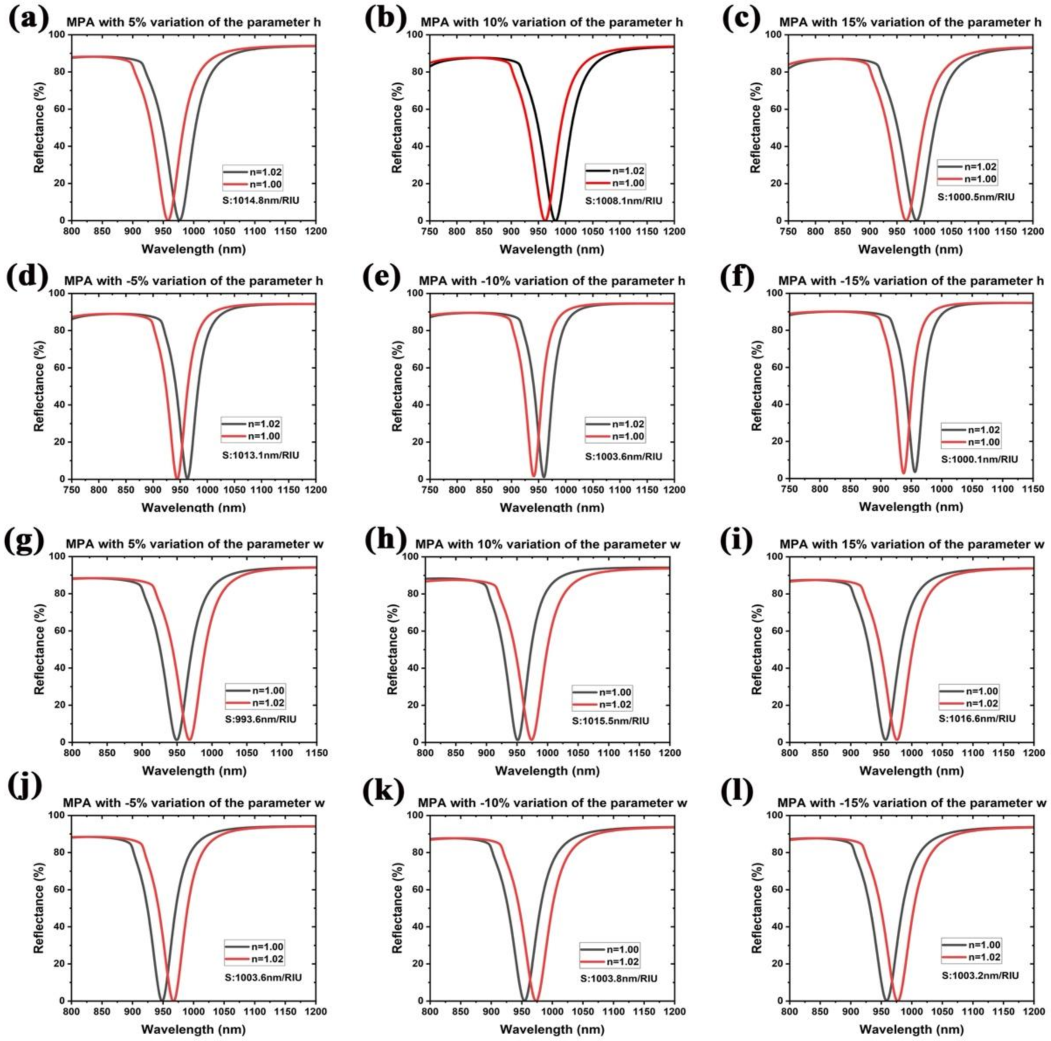

Figure S5. Calculated reflectance spectra of the BMA for different values of h (a-f), w (g-l) under varied refractive index, together with the corresponding sensitivities. Because the sensing mode exhibits a narrow linewidth of approximately 23 nm, even modest fabrication errors may influence the resonance response. To evaluate the robustness of the design under realistic dimensional deviations, we therefore performed a tolerance analysis on two representative structural parameters that are expected to be critical in fabrication: the ZrN layer thickness and the lateral feature width. Each parameter was independently varied from -15% to +15% relative to the optimized design, while the resonance wavelength, absorptivity, and refractive-index sensitivity were extracted for comparison. The corresponding results are summarized in Fig. S6 and Tables S5-S6.

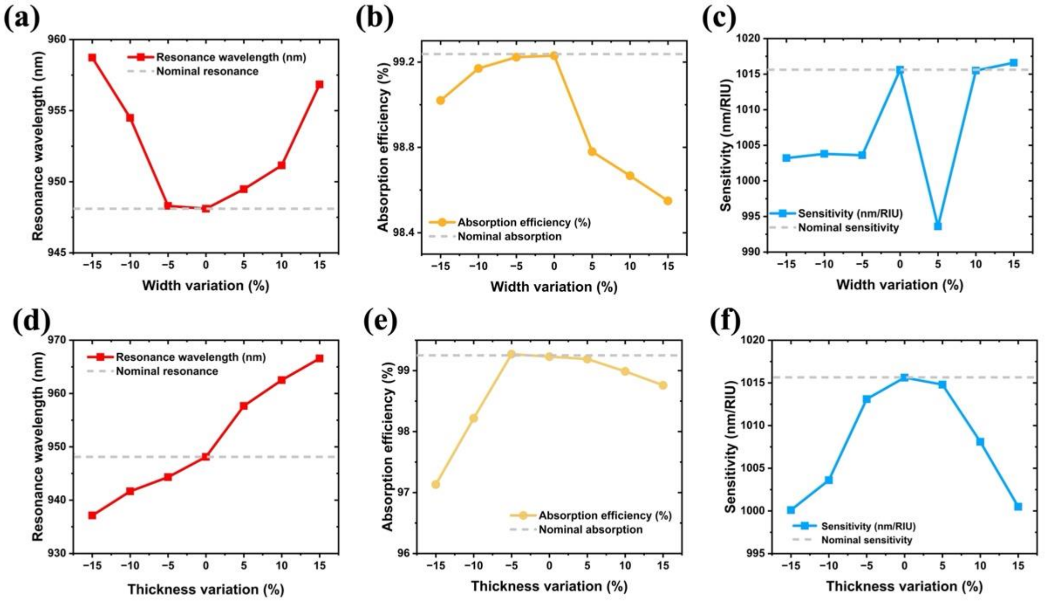

Figure S6. Dimensional tolerance analysis of the proposed sensor. Dependence of resonance wavelength, absorptivity, and refractive-index sensitivity on (a-c) thickness variation and (d-f) width variation from -15% to +15% relative to the nominal design. The results show that thickness is the more sensitive parameter for the resonance position, whereas the absorptivity and sensitivity remain robust under moderate dimensional deviations.

Table S5. Simulated influence of thickness variation on the resonance wavelength, absorptivity, and refractive-index sensitivity of the proposed sensor

Thickness variation (%)	Resonance wavelength (nm)	Absorptivity (%)	Sensitivity (nm/RIU)
-15	937.12	97.13	1000.1
-10	941.64	98.21	1003.6
-5	944.31	99.27	1013.1
0	948.10	99.23	1015.6
5	957.67	99.19	1014.8
10	962.50	98.98	1008.1
15	966.57	98.75	1000.5

Table S6. Simulated influence of width variation on the resonance wavelength, absorptivity, and refractive-index sensitivity of the proposed sensor

Width variation (%)	Resonance wavelength (nm)	Absorptivity (%)	Sensitivity (nm/RIU)
-15	958.72	99.02	1003.2
-10	954.49	99.17	1003.8
-5	948.30	99.22	1003.6
0	948.1	99.23	1015.6
5	949.47	98.78	993.6
10	951.14	98.66	1015.5
15	956.84	98.54	1016.6

As shown in Fig. S6(a-c) and Table S5, variation in thickness significantly affects the resonance position. When the thickness deviation changes from -15% to +15%, the resonance wavelength shifts from 937.12 to 966.57 nm, corresponding to a total variation of about 29.45 nm. In contrast, the absorptivity remains consistently high, ranging from 97.13% to 99.27%, while the refractive-index sensitivity varies only slightly from 1000.1 to 1015.6 nm/RIU. These results indicate that the sensing resonance is moderately sensitive to thickness errors, whereas the absorption strength and sensing capability remain largely preserved.

A similar analysis was performed for width variation, as shown in Fig. S6(d-f) and Table S6. Compared with thickness, the resonance wavelength exhibits a smaller overall change under width deviation, remaining within the range of 948.10-958.72 nm. Meanwhile, the absorptivity is maintained above 98.5% for all cases, and the sensitivity remains close to 1000 nm/RIU, varying only between 993.6 and 1016.6 nm/RIU. This suggests that the proposed structure is relatively tolerant to moderate lateral dimension errors. To further illustrate the spectral evolution, the calculated reflectance spectra for different values of thickness and width under varying refractive indices are presented in Fig. S5. In both cases, the resonance dip remains well defined as the refractive index changes, and the corresponding resonance shift is preserved, confirming that the sensing function is robust against moderate geometric perturbations. Overall, these results demonstrate that although the resonance wavelength is somewhat more sensitive to thickness variation than to width variation, the proposed sensor maintains high absorptivity and stable refractive-index sensitivity under realistic fabrication tolerances, supporting its experimental feasibility.

REFERENCES

1. Rahad, R.; Haque, M.A.; Mahadi, M.K.; Mohsin, A.S.; Faruque, M.O.; Afrid, S.M.T.-S.; Emon, M.J.H.; Sagor, R.H. Highly sensitive optically tunable transition metal nitride-based plasmonic pressure sensor with CMOS-compatibility at compact subwavelength dimensions. *IEEE sensors journal* **2024**, *24*, 22271-8. DOI: 10.1109/JSEN.2024.3404479